Analysis of Flame Stabilization to a Photovoltaic Micro-Combustor Step in Turbulent Premixed Hydrogen Flame

Bahamin Bazooyar[1]

Hamidreza Gohari Darabkhani[2,*]

School of Engineering and Creative Art, Staffordshire University, Stoke-on-Trent,

ST4 2DE, United Kingdom

[1]Bahamin Bazooyar, Research Fellow in Turbulent Combustion (Bazooyar.bb@gmail.com)

[2,*]Corresponding author: Hamidreza Gohari Darabkhani, Professor of Low Carbon and Renewable Energy Systems

Email: h.g.darabkhani@staffs.ac.uk

Tel: +44 (0) 1782 292769

ABSTRACT: One of the effective strategies in meso and micro combustors for flame stabilization is to consider a wall cavity in a step. This extends the blow-off limit that can cause flame stagnation and anchoring. In the present work, the premixed hydrogen turbulent flame in a photovoltaic combustor with a step is simulated, validated and researched in terms of flame stabilization at different operating points including jet temperature, velocity, hydrogen, nitrogen, water content, and equivalence ratios. The effect of preferential transport of species is also evaluated and discussed. The results of simulations were employed to investigate the flame anchoring by showing the interplay between the flow field, heat recirculation, elementary reactions, transport of species. The results confirm that in this combustor the fresh reactant is gradually heated by the channel walls. This shifts the threshold of the combustion to the vicinity of the microchannel interior walls and more intense combustion downstream. The combustion in partially reacted materials is intensified by passing the duct interior walls when it faces the recirculating materials in the channel cavity leading to flame anchoring and stabilization from the cavity wall. The flame anchoring mechanism in this channel is the heat recirculation via channel walls, recirculating materials, and radical pool in the channel cavity for premixed hydrogen/oxygen flame. The effect of heat recirculation is found dominant in flame anchoring as in most case studies the flame stabilizes and evolves from the duct interior walls. The heat transferred to fresh reactant was 140, 129, 127, and 77 kW/m^2 in Inconel, Stainless Steel, Silicon Carbide, and Quartz combustor, respectively.

Keywords: hydrogen, micro-combustion, flow field, recirculation zone, flame anchoring.

Symbols	
A	surface area
Cp	constant pressure thermal conductivity
d	Diameter [m]
E_f	Fluid energy [J]
h	Enthalpy [J. mol^{-1}]
h_o	Heat transfer coefficient [W/m^2 K]
I	Unit matrix
J	Molecular diffusion flux
$\vec{J}$	Diffusion flux vector
k	thermal conductivity [W/m K]
k_n	Knudsen number

l	length [m]
l^*	characteristic length [m]
p	pressure [pa]
Q	Thermal flux [kW/m^2]
R	Production rate of chemical reactions [mol. m^{-3}. s^{-1}]
S	source term
Re	Reynolds number
Sc	Schmidt number
T	Temperature [K]
u	Velocity vector [m.s^{-1}]
X	Mole fraction
Y	Mass fraction

Greek letters

r	Density [kg. m^{-3}]
l	Mean free path [m]
e	Dissipation rate [m^2. s^{-2}]
μ	Fluid viscosity
e	Emissivity
s	Stephan Boltzman constant
n	Kinematic viscosity
G	Diffusivity coefficient

Subscripts

i, j, k	Species indices
eff	effective
ave	average
w	wall
w, i	wall inlet
w, o	wall outlet

Superscript

h	enthalpy
T	transpose

Abbreviation

AARD	Average absolute relative deviation
NO$_X$	Nitrogen oxides
RANS	Reynolds-Averaged Navier-Stokes
MEMS	Micro-Electro-Mechanic-Systems
TPV	micro thermo-photovoltaic
PRESTO	PREssure Staggering Option
PISO	Pressure Implicit with Split Operator
EDC	Eddy Dissipation Concept
ER	Equivalence Ratio
STD	Standard deviation
RMSE	Root mean square error

1. Introduction

The rapid industrialization of the world necessitates the use and application of Micro-Electro-Mechanic-Systems (MEMS) including micro-turbines, robots, satellites and other portable electric devices [1]. The meso and microscale combustion systems are now emerging and being developed to power the MEMS, largely because combustion provides more energy density, longer life spans, without any recharging periods compared with electric devices [2]. The use of combustor at small scales is almost challenging and not completely devoid of any in situ problems. The flame stability, heat loss because of the high surface to volume areas [3], and short residence time currently hinder the operability of meso micro combustors necessitating the tremendous effort to improve the combustion in these small scale combustors. The combustor structural design [4], management and optimization of heat recirculation and heat loss control [5-7], the recirculation zone [8] and low-velocity zone establishment [9-11] are effective strategies to compensate for the negative effect of heat loss and thus sustain stable flames in micro-scale combustors. The use of catalytic porous medium [12-14] and the use of cavity are among structural considerations to stabilize flame in micro-combustors. The use of cavity in the micro combustors can establish the recirculation zone, reduce the heat loss and preheat the incoming fresh mixture, thereby stabilizing the flame at the micro scales. Although these structural design amendments have stabilized the flames, they may lead to some operational problems in small scale combustors. The flame anchoring and as a result attaching to the combustor walls can melt the sensitive small walls of the micro-combustor.

The use of hydrogen fuel in microscale combustors seems to be extremely interesting as this potential fuel has high heating value and a small quenching distance [15, 16]. The micro-combustors can be suitably fueled with hydrogen fuel without giving off any carbon emissions. Blow-off limits of micro combustor are several times larger than the corresponding burning velocities of H_2/air mixtures, leading to "flame tip-opening phenomenon" [17, 18]. This can improve the combustion stability of hydrogen significantly and be a prerequisite in micro thermo-photovoltaic (TPV) systems or micro-propulsion systems. Despite the potential benefits of using hydrogen fuel in micro-

combustor in terms of carbon emissions and stability, this fuel should be effectively stabilized in micro-combustors. Li et al. [19] applied the cavity flame holder with a segmented catalyst on the interiors of micro-channel to stabilize the hydrogen flame. They revealed that the cavities could stabilize the operation of microreactors at a wider range of inlet flow velocities. Wan et al. [20] that "the small cavity-combustor could be potentially used for micro thermo-photovoltaic (TPV) systems or micro-propulsion systems". The cavities could even improve the reaction rates in combustion. Nehe and Kumar [21] pointed out that the use of cavity improves the hydrogen production in the methanol reforming conversion rate. Faramarzpour et al. [22] showed that the use of a cavity in the micro-combustor increases the blowout limit and mean wall temperature. Peng et al. [23] have also demonstrated that length and the wall thickness of micro combustors plays a pivotal role in the flame stabilization and they guessed that is because of the recirculation of materials in the vicinity of step wall. However, the mechanism of flame stabilization in micro combustors is still unknown. In the present work, the anchoring mechanisms of a premixed hydrogen/air flame in a photovoltaic microchannel combustor are presented and analyzed by demonstrating the interactions among the flow field, heat recirculation, transport of preferential species and rate of elementary reactions contributing to the flame stabilization. To this end, the turbulent combustion of premixed H_2/O_2 flame is simulated using Reynold-Average-Navier-Stokes (RANS)/eddy dissipation concept (EDC) numerical algorithm using direct integration from chemical reactions. The influence of different operating points (equivalence ratio, jet temperature, hydrogen, oxygen, nitrogen, and water content) is investigated through 24 numerical simulations. The effect of different solid materials is also tested in flame anchoring mechanism and combustion stabilization. The flame anchoring mechanism of hydrogen flame has been analyzed in other combustors by Wan et al. [24],we have used their strategy to show these mechanisms in a photovoltaic micocombustor.

2. Simulation of the micro combustor

2.1 Geometry

Fig 1 depicts the schematic of the micro-combustor. It is a cylindrical channel with a step. The length of the channel (l_2) is 18 mm and length of step 0.5 mm. The entrance of the combustor channel is 2 mm long (l_1) with a smaller diameter compared to the outlet. The inner diameter of micro combustor at the inlet d_1 and at the outlet d_2 are 2.0 mm and 3.0 mm, respectively. The outer diameter of the microchannel is 4.0 mm. The change in diameter is by a sudden expansion using a vertical step. The premixed mixture of hydrogen/air is injected from the smaller inlet surface and the exhaust gas comes out of the larger outlet surface. The stainless steel material was used to proceed with the modeling as the basic material at different operating points: r = 8030 kg/m³, C_P = 502.48 J/kg.K, k = 16.27 W/m.K.
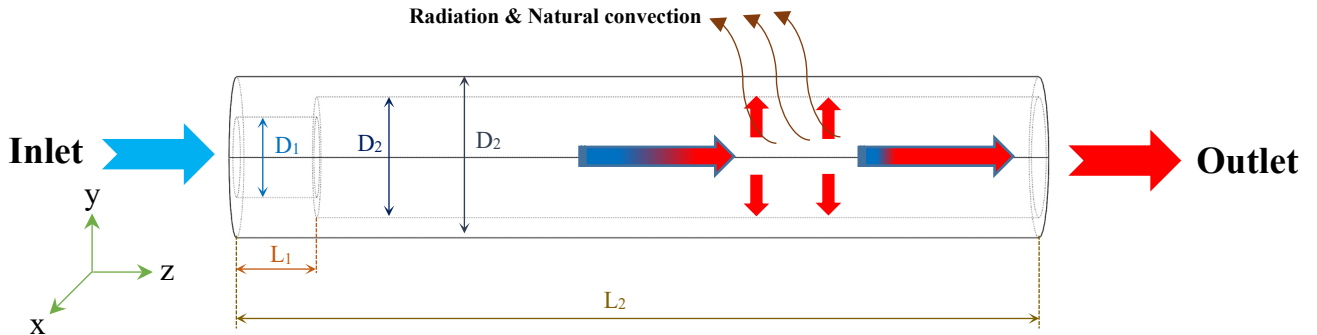
Fig 1 The schematic of the micro combustor

3. Model formulation

The initial estimation of Knudsen number ($K_n = l/l^*$) in the combustor showed that the mean free path of H_2 and O_2 (l) is significantly lower than the characteristics length (l^*) of the microchannel and much less than the critical value 10^{-3}. Thus, the fluid in the microchannel can be considered as a continuum and the Navier-Stokes equation can be satisfactorily applied for the momentum balance.

The conservation equations of mass, momentum, and energy are achieved using a steady-state solver with these assumptions that 1) no Dufour effects, 2) no work by pressure and viscous forces, 3) no surface reactions and 4) no gas radiation are present in the micro-combustor.

The mass balance is:

$$\nabla \cdot \left(\rho \vec{u} \right) = 0 \tag{1}$$

where ρ and $\vec{u}$ denote the gas density and velocity vector, respectively.

The momentum balance is:

$$\rho \left(\vec{u} \cdot \nabla \vec{u} \right) = -\nabla p + \nabla \cdot \left[\mu \left(\nabla \vec{u} + \left(\nabla \vec{u} \right)^T \right) - \frac{2}{3} \nabla \cdot \vec{u} I \right] \tag{2}$$

where p, μ and I indicate the absolute pressure, molecular viscosity, and unit tensor, respectively.

The energy balance is:

$$\nabla \cdot \vec{u} \left(\rho E_f + p \right) = \nabla \cdot \left[k_{eff} \nabla T - \left(\sum_j h_j \vec{J}_j \right) + \left(\mu \left(\nabla \vec{u} + \left(\nabla \vec{u} \right)^T \right) - \frac{2}{3} \nabla \cdot \vec{u} I \right) \cdot \vec{u} \right] + S_f^h \tag{3}$$

where T represents the temperature, E_f is total fluid energy, k_{eff} denotes the effective conductivity, $\vec{J}_j$ and h_j show the diffusion flux and enthalpy of species j, and S_f^h denotes fluid enthalpy source term.

At the micro combustor wall, the energy balance should be established:

$$\nabla \cdot \left(k_w \nabla T \right) = 0 \tag{4}$$

where k_w is the thermal conductivity of the wall.

To model the combustion, the conservation of species is required:

$$\nabla \left(\rho \vec{u} Y_j \right) = -\nabla \vec{J}_j + R_j \tag{5}$$

In this equation, Y_j and R_j denote the mass fraction and the net production rate of the specie j in chemical reactions.

To solve the governing equations, the k-ε is employed to model the turbulence. The eddy dissipation concept (EDC) is exploited to handle turbulent/chemistry interactions. The direct integration scheme from chemical reactions is used in species transport equations. The chemical reactions are obtained from Li [25] hydrogen combustion mechanism. For nitrogen chemistry, 13 additional reactions were

added to the Li combustion mechanism including NO formation from the thermal mechanism and N$_2$O pathways, and reactions corresponding to the formation and destruction of NO$_2$. The Fenimore mechanism from the considered reactions. Prompt NO is not available in this analysis as no hydrocarbon exists in the hydrogen turbulent flame [26-29].

The list of elementary chemical reactions for the hydrogen flame is all listed in table 1.

Table 1 N$_2$/H$_2$/O$_2$ combustion mechanism, $k = AT^n \exp(-E/RT)$.

NO	Reaction		A (cm, mol, s)	n	E (kcal mol^{-1})
(R1)	$H + O_2 \rightleftharpoons O + OH$		3.55×10^{15}	-0.41	16.6
(R2)	$O + H_2 \rightleftharpoons OH + H$		5.08×10^{04}	2.67	6.29
(R3)	$H_2 + OH \rightleftharpoons H_2O + H$		2.16×10^{08}	1.51	3.43
(R4)	$O + H_2O \rightleftharpoons OH + OH$		2.97×10^{06}	2.02	13.4
(R5)	$H_2 + M \rightleftharpoons H + H + M$		4.58×10^{19}	-1.40	104.38
(R6)	$O + O + M \rightleftharpoons O_2 + M^a$		6.16×10^{15}	-0.500	0.00
(R7)	$O + H + M \rightleftharpoons OH + M^a$		4.71×10^{18}	-1.00	0.00
(R8)	$H + OH + M \rightleftharpoons H_2O + M^a$		3.80×10^{22}	-2.00	0.00
(R9)	$H + O_2 + M \rightleftharpoons HO_2 + M^b$	k_0	6.37×10^{20}	-1.72	0.52
		k_∞	1.48×10^{12}	0.60	0.00
(R10)	$HO_2 + H \rightleftharpoons H_2 + O_2$		1.66×10^{13}	0.00	0.82
(R11)	$HO_2 + H \rightleftharpoons OH + OH$		7.08×10^{13}	0.00	0.30
(R12)	$HO_2 + O \rightleftharpoons OH + O_2$		3.25×10^{13}	0.00	0.00
(R13)	$HO_2 + OH \rightleftharpoons H_2O + O_2$		2.89×10^{13}	0.00	-0.50
(R14)	$HO_2 + HO_2 \rightleftharpoons H_2O_2 + O_2^c$		4.20×10^{14}	0.00	11.98
	$HO_2 + HO_2 \rightleftharpoons H_2O_2 + O_2$		1.30×10^{11}	0.00	-1.63
(R15)	$H_2O_2 + M \rightleftharpoons 2OH + M^d$	k_0	1.20×10^{17}	0.00	45.5
		k_∞	2.95×10^{14}	0.00	48.4
(R16)	$H_2O_2 + H \rightleftharpoons H_2O + OH$		2.41×10^{13}	0.00	3.97
(R17)	$H_2O_2 + H \rightleftharpoons HO_2 + H_2$		4.82×10^{13}	0.00	7.95
(R18)	$H_2O_2 + O \rightleftharpoons OH + HO_2$		9.55×10^{06}	2.00	3.97
(R19)	$H_2O_2 + OH \rightleftharpoons HO_2 + H_2O^c$		1.00×10^{12}	0.00	0.00
	$H_2O_2 + OH \rightleftharpoons HO_2 + H_2O$		5.80×10^{14}	0.00	9.56
(R20)	$N + NO \rightleftharpoons N_2 + O$		3.50×10^{13}	0.00	0.33
(R21)	$N + O_2 \rightleftharpoons NO + O$		2.65×10^{12}	0.00	6.40
(R22)	$N + OH \rightleftharpoons NO + H$		7.333×10^{13}	0.00	1.12
(R23)	$NO + NO \rightleftharpoons N_2 + O_2$		3.00×10^{11}	0.00	65.0
(R24)	$N_2O + O \rightleftharpoons N_2 + O_2$		1.40×10^{12}	0.00	10.810

(R25)	$N_2O + O \rightarrow NO + NO$	2.90×10^{13}	0.00	23.15
(R26)	$N_2O + H \rightarrow N_2 + OH$	4.40×10^{14}	0.00	18.88
(R27)	$N_2O + OH \rightarrow N_2 + HO_2$	2.00×10^{12}	0.00	21.06
(R28)	$N_2O + M \rightarrow N_2 + O + M$	1.30×10^{11}	0.00	59.62
(R29)	$NO + HO_2 \rightarrow NO_2 + OH$	2.11×10^{12}	0.00	-0.48
(R30)	$NO + O + M \rightarrow NO_2 + M$	1.06×10^{20}	-1.41	0.00
(R31)	$NO_2 + O \rightarrow NO + O_2$	3.90×10^{12}	0.00	-0.24
(R32)	$NO_2 + H \rightarrow NO + OH$	1.32×10^{14}	0.00	0.360

[a] Efficiency factor for $\varepsilon_{H_2O} = 12$ and $\varepsilon_{H_2} = 12$.

[b] Troe parameter is F_c=0.8. Efficiency factor for $\varepsilon_{H_2O} = 12$. Efficiency factor for $\varepsilon_{H_2O} = 11$, $\varepsilon_{H_2} = 2$ and $\varepsilon_{O_2} = 0.78$.

[c] (R14) and (R19) are expressed as the sum of the two rate expressions.

[d] Troe parameter is F_c=0.5. Efficiency factor for $\varepsilon_{H_2O} = 12$ and $\varepsilon_{H_2} = 2.5$.

The properties of fuels [30-33] could affect the combustion and accuracy of the simulations. The properties of the combustion mixture including all species are needed for the simulations. The density and specific heat are considered by incompressible-ideal-gas and mixing laws [34, 35], respectively. The specific heat of each component is obtained from a piecewise polynomial fitting of temperature. The viscosity and thermal conductivity are determined from the mass fraction-weighted mean of all species [36, 37].

The hydraulic diameter and turbulent intensity at the inlet for all operating points are 2 mm and 5%, respectively. The pressure-outlet boundary type is used at the outlet. At the outlet, the turbulent intensity and hydraulic diameter are 5% and 3 mm, respectively. At the micro-combustor walls, no-slip condition and zero diffusive flux are employed to handle the gas-solid interfaces. The walls at the left and right side of the combustor are assumed adiabatic. The convective and radiative mechanisms of heat transfer with the ambient are considered at the outer wall. The equation for the heat loss is:

$$Q_{loss} = h_0 \sum A_i \left(T_{w,i} - T_o\right) + \varepsilon\sigma \sum A_i \left(T_{w,i}^4 - T_0^4\right) \tag{6}$$

In this equation, A_i indicates the surface area of grid cells, $T_{w,i}$ denotes the temperature at the grid cells of the walls, σ represents the Stephan-Boltzmann constant, $5.67 \times 10^{-8} \ W/\left(m^2 K^4\right)$, h_0 is the

heat transfer coefficient, 10 $W/(m^2K)$ for natural convection heat transfer and 32 $W/(m^2K)$ for turbulent convection heat transfer, and e indicates the wall emissivity, 0.85.

In the finite volume part of the model, a steady segregated solver is used with the implicit formulation. A second-order upwind scheme is applied for space derivatives of advection terms in the transport equations and, PRESTO (PREssure Staggering Option) and PISO (Pressure Implicit with Split Operator) algorithms are employed for pressure and pressure-velocity coupling, respectively. The residuals for continuity, momentum, and transport of species are set 10^{-3} to obtain convergence in the solution. For the energy equation, the residual criterion is set 10^{-6}. A monitor including the area-averaged temperature at the micro-combustor outlet is defined to assure the completion of the simulation. The simulation is initiated by the "temperature patch=2000 K" at the entire domain including both solid and fluid. The simulations are considered complete at each operating point when the area-averaged-total-temperature at the outlet was constant and the residuals of the differential equations met the pre-defined conditions.
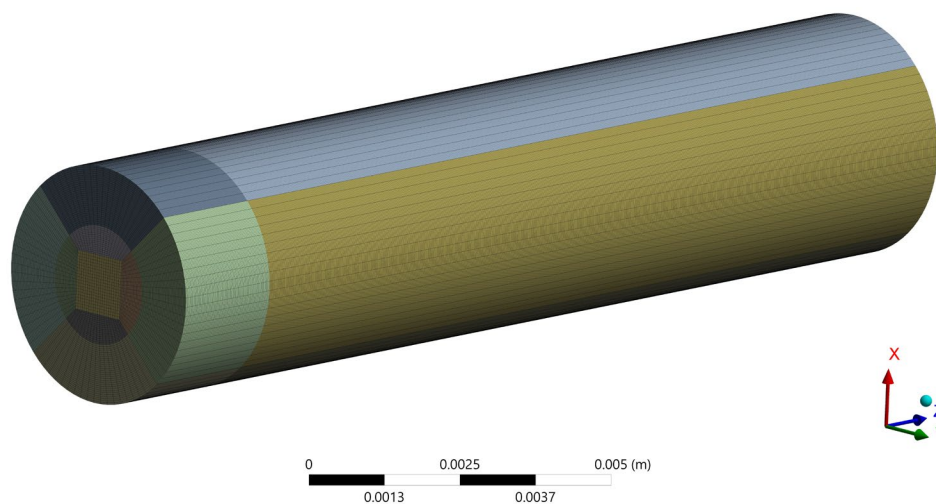
Fig 2 The computational domain including structured grids

Before the final post-processing of the results, several numbers of gird mesh are tested starting with 524,546 to 5,890,285 cells. The mesh was uniform and structured with high orthogonality to obtain a better convergence in differential equations. The computational domain is depicted in Fig 2. Our preliminary analysis has shown that by increasing the grids to a number of more than 3.2 million, the

variation in results is less than 5%. Consequently, 3.2 million grids are considered optimum in obtaining the required accuracy and saving computational costs.

4. Operating conditions

The temperature, proportion of hydrogen to air, the turbulence intensity, and impurities in the fuel stream (i.e., water, inert gases) could influence the anchoring location of the flame. To analysis this phenomenon, 24 operating points are defined in the fuel jet. Table 2 gives the operating conditions. The hydrogen jet temperature, velocity, oxygen content, nitrogen content, water addition when it replaces both hydrogen and oxygen, and equivalence ratio has been thoroughly considered for this analysis. In addition, different combustor materials are also tested to show the effect of combustor heat recirculation on flame stabilization.

Table 2 Operating conditions for hydrogen combustion in thermophotovoltaic micro combustor

No.	Jet					
	u (m/s)	T (K)	x_{H_2}	x_{O_2}	x_{N_2}	x_{H_2O}
1[a]	5	300	0.2942	0.1483	0.5575	0[a]
2		350				
3		400				
4		500				
5	7.5					
6	10					
7	15					
8			0.3942		0.4575	
9			0.4942		0.3575	
10			0.3442	0.0983		
11			0.3442		0.5075	
12				0.0983		0.05
13					0.5075	0.05
14					0.4575	0.1
15					0.3575	0.2

16			0.1736	0.1736	0.6529
17			0.2013	0.1677	0.6310
18			0.2272	0.1623	0.61051
19			0.3866	0.1288	0.4847

<div align="right">
All compositions are mole fractions.
[a] Base case.
Empty place means that the operating point is the same as the base case.
</div>

5. Validation

This model was previously validated against experimental data in two precedent analysis [38, 39]. Similar results are obtained here. There is some difference between the experimental and model data as in previous studies. The influence of different combustion mechanisms is also verified here as in [40]. The statistical errors of different combustion mechanisms in the prediction of experimental values are compared in table 3. This table shows the error of simulations for the temperature at the outer wall of the microchannel. The difference between the modeling and experimental data is partly due to measurements and partly because of the mathematical models including RANS formulation, the choice of combustion mechanism, etc. The maximum relative error is around 10% upstream of the jet flow which is going down downstream of the fuel nozzle. There, the relative error is around 1.6%.

Table 3 The statistical errors of the combustion mechanisms

No	Mechanism	Ref	Species no (orig.)	Reactions no (orig.)	Statistical errors		
					%AARD	RMSE	STD
1	Li-2007	[25]	11(21)	25(93)	3.25	49.5	89.9
2	Kéromnès-2013	[41]	12(17)	33(49)	5.53	97.5	115
3	ÓConaire-2004	[42]	10	21	4.21	79.1	81.7
4	Konnov-2008	[43]	10	33	4.81	90.7	99.2
5	Hong-2011	[44]	10	31	5.58	100	121
6	Davis-2005	[45]	11(14)	25(38)	4.88	89.1	98.2

| 7 | Bruke-2012 | [46] | 11 | 27 | 5.92 | 103 | 127 |

7. Results and discussion

   In this section, the results obtained from the simulations are discussed and interpreted. For hydrogen turbulent flame in the micro-combustor, the influence of different parameters including temperature, water content, hydrogen, nitrogen and oxygen content of the jet, and finally the equivalence ratio of the fuel stream is analyzed using contour plots of H mass fraction and velocity lines. The H radical is the marker of the flame front as it shows the reactive zone of the hydrogen flame. The velocity lines are employed to analyze the combustion species path lines in the combustor.

Fig 3 demonstrates the colored contours of H radical mass fraction overlaid by velocity for five equivalence ratios: 0.5 in run 16 (Fig 3-(a)); 0.6 in run 17 (Fig 3-(b)); 0.7 in run 18 (Fig 3-(c)); 1 in run 1 (Fig 3-(d)); 1.5 in run 19 (Fig 3-(e)). The flame anchoring root is observed at the duct of the microchannel prior to the step for runs 1, 18 and 19. At these operating points, the flame formed before the microchannel step near the interior horizontal walls. Near the combustor wall, the fluid is nearly stagnant full of precursor species. This forms a radical pool for chemical reactions. When equivalence ratio becomes lower (for runs 16 and 17), the amount of hydrogen in the fuel jet gets fewer leading to the formation of flame further downstream. At these conditions, the flame root is anchored to the step vertical wall for whatever the investigated equivalence ratio. Here, the heat recirculation in the microchannel cavity leads to the flame evolution from the step walls. Indeed, there is a recirculation zone established in the vicinity of the step wall full of combustion species, as a result, forming a radical pool for the ignition and flame stabilization.

(a) Run 16: equivalence ratio=0.5

(b) Run 17: equivalence ratio=0.6

(c) Run 18: equivalence ratio=0.7

(d) Run 1: test case equivalence ratio=1

(e) Run 19: equivalence ratio=1.5
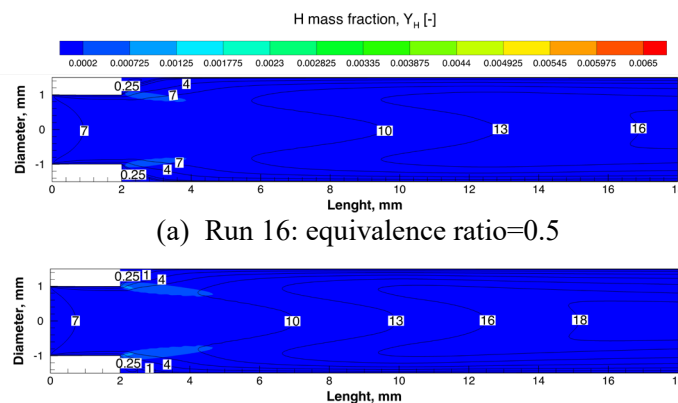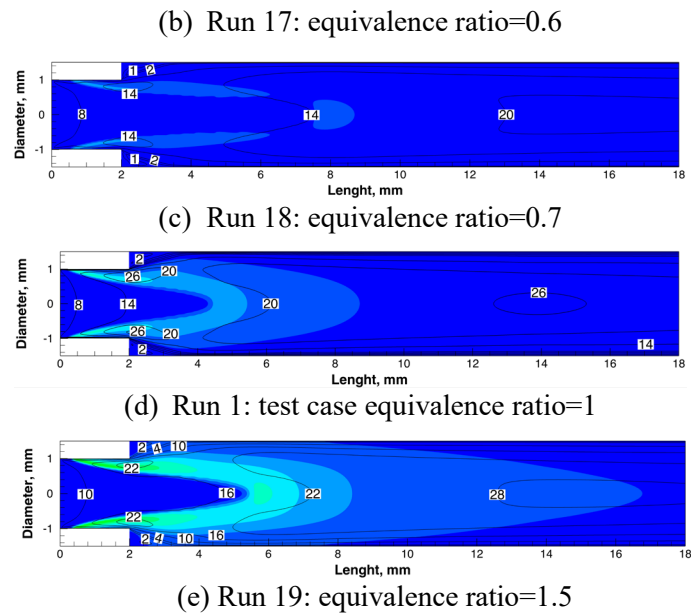
Fig 3 Colored contours of mass fraction of radical H with overlaid velocity level lines (black line) at equivalence ratio 0.5, 1 and 1.5 (combustor material= stainless steel)

7.1 Effect of operating points

The flame anchoring at different operating points are shown in two groups and depicted in Figs 4, 5 and 6. Fig 4 gives the contour plots obtained at different jet temperature, velocity, hydrogen, water content, and equivalence ratio. Fig 5 draws an analogy between the two cases: when the hydrogen and water replace either the nitrogen or oxygen. Fig 6 gives a closer look at the role of the recirculation zone established the microchannel cavity for the flame anchoring.
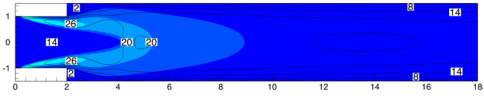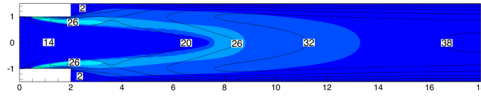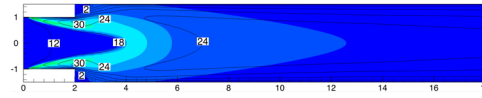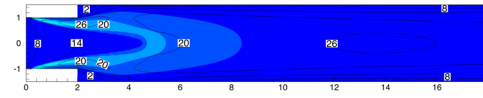
(b) Run 2: $T_j = 350$ K

(c) Run 3: $T_j = 400$ K

(d) Run 4: $T_j = 500$ K

(e) Run 5: $v_j = 7.5\ m/s$

(f) Run 6: $v_j = 10\ m/s$

(g) Run 7: $v_j = 15\ m/s$

(h) Run 11: $x_{H_2,j} = 0.3442$

(i) Run 8: $x_{H_2,j} = 0.3942$

(j) Run 9: $x_{H_2,j} = 0.4942$

(k) Run 13: $x_{H_2O,j} = 0.05$
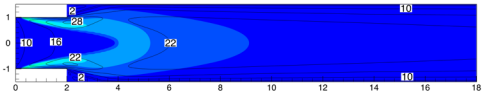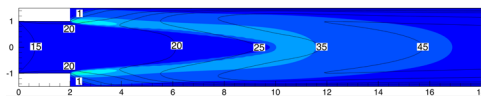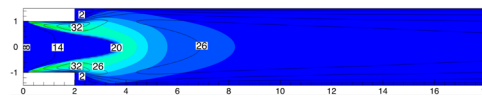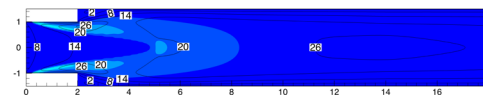
(l) Run 14: $x_{H_2O,j} = 0.1$
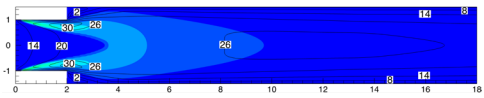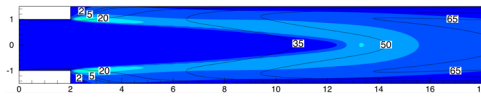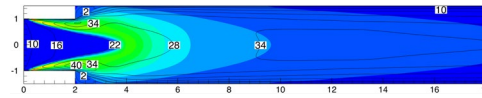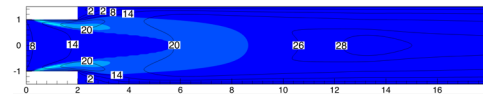
(m) Run 15: $x_{H_2O,j} = 0.2$

Fig 4. Colored contours of mass fraction of radical H with overlaid velocity level lines (black line) at different operating points.

The flame anchoring for most of the cases appears at the duct of microchannel interior walls, although the flame reactivity and velocity profiles slightly changed. The inlet velocity of hydrogen and air mixture can only change the place of flame anchoring to the microchannel step (in operating points tested in Fig 4). When the velocity transcends the 7.5 m/s, the evolution of H radicals is observed from the cavity of the microchannel. The high jet velocity pushes the flame radicals to the extended area of the microchannel where they can now recirculate towards the step walls. The flame anchoring root at higher jet velocities is observed near the hot step vertical wall. At higher jet velocities, the recirculation zone is stronger creating the potential for a part of the flow to move backward near the step, thereby anchoring the flame to the step wall.

Fig 5 makes a comparison when water and hydrogen replace either the nitrogen or oxygen. As the concentration of oxygen is lowered, either it is replaced with hydrogen or water (Fig 5-(b)-(d)), the flame anchoring place shifts to the cavity of the microchannel. This shift in place of anchoring flame cannot be observed when the hydrogen and water replace the nitrogen (Fig 5-(c)-(e)). Indeed, the lack of oxygen in the premixed mixture of fuel and air necessitates more residence time for the reactants and high temperature for ignition. At this condition, the initiation of chemical reactions begins in the microchannel where radical species recirculate, and wall temperature is high enough for combustion. When the hydrogen and water take the place of hydrogen (Fig 5-(b)-(d)), the flame anchors to the duct interior walls. In this case, the oxygen in the jet stream is high enough for the beginning of combustion elementary reactions at a comparatively lower temperature than the previous case studies.
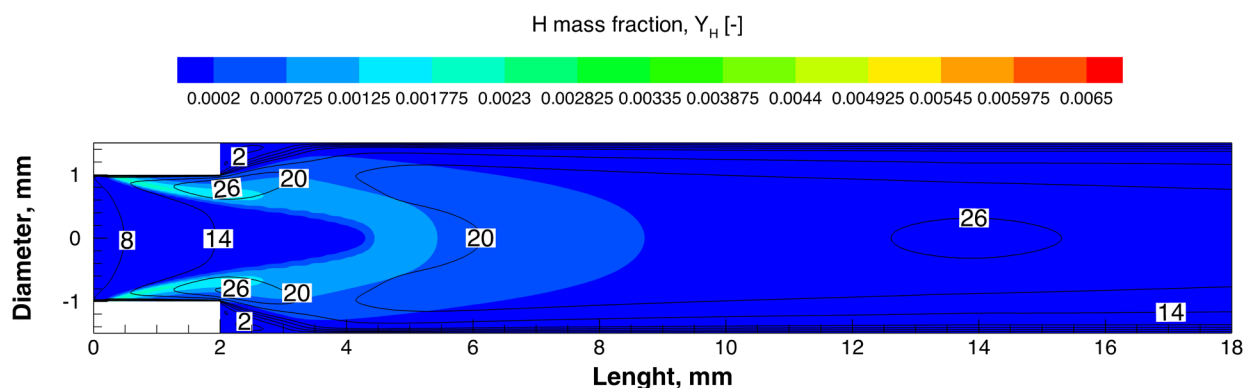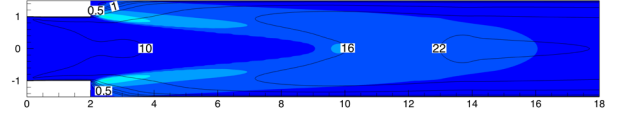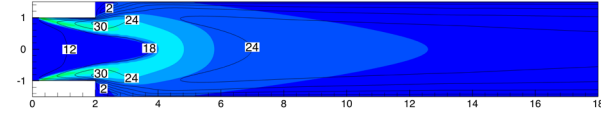
(a) Test-case run 1: $x_{H_2,j}$ = 0.2942, $x_{O_2,j}$ = 0.1483, $x_{N_2,j}$ = 0.5575, $x_{H_2O,j}$ = 0
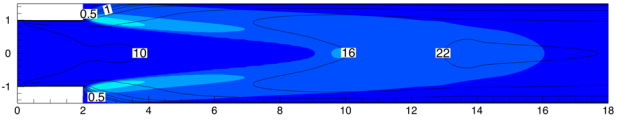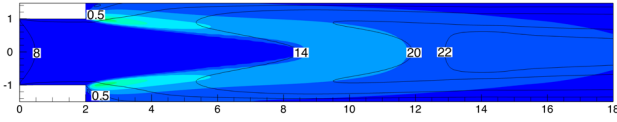
(b) Run 10: $x_{H_2,j}$ = 0.3442, $x_{O_2,j}$ = 0.0983, $x_{N_2,j}$ = 0.5575

(d) Run 12: $x_{H_2O,j}$ = 0.05, $x_{O_2,j}$ = 0.0983, $x_{N_2,j}$ = 0.5575
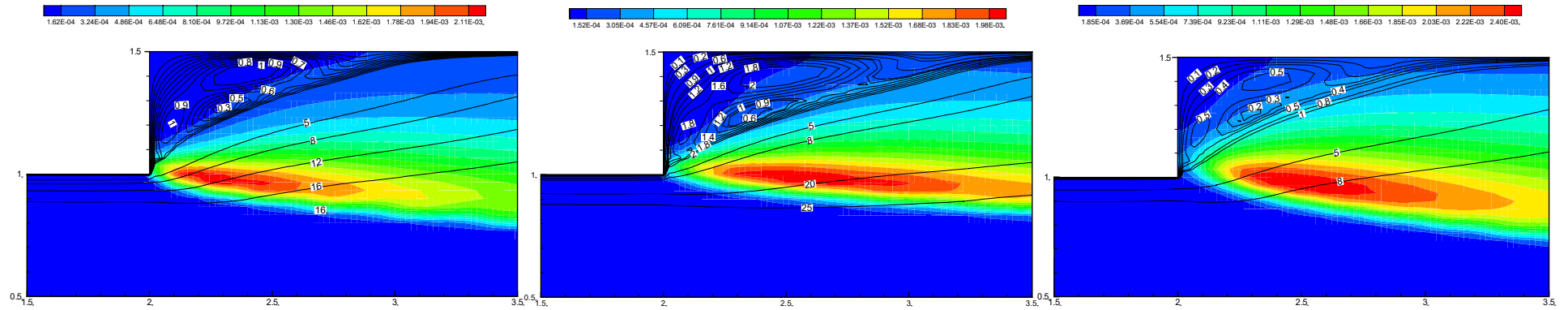

(c) Run 11: $x_{H_2,j}$ = 0.3442, $x_{O_2,j}$ = 0.1483, $x_{N_2,j}$ = 0.5075

(e) Run 13: $x_{H_2O,j}$ = 0.05, $x_{O_2,j}$ = 0.1483, $x_{N_2,j}$ = 0.5075

Fig 5. Colored contours of mass fraction of radical H with overlaid velocity level lines (black line) when hydrogen and water replace oxygen

As discussed above, the flame anchoring is observed in the proximity of step vertical walls at higher jet velocities (runs 6 and 7), lower equivalence ratios (runs 16 and 17) and as water and hydrogen is replaced with of oxygen (runs 10 and 12) that was otherwise on the interior microchannel duct walls for other operating points. To investigate the flame anchoring more closely, the mass fraction distribution of H overlaid by velocity level lines near the flame tip is demonstrated in Fig 6. For the operating points given, the flame is anchored by the recirculation zone near the vertical wall of the cavity where there is a low-velocity fluid in high temperatures. Indeed, the counterflow established near the microchannel step recirculates the species. This increases the residence time of the combustion species, thereby developing a radical pool for chemical reactions. The backward flow in the vicinity of step vertical wall via recirculation zone curtails the flame root from being moving downstream. This anchors the flame to the step vertical wall and flame stabilization from this area.
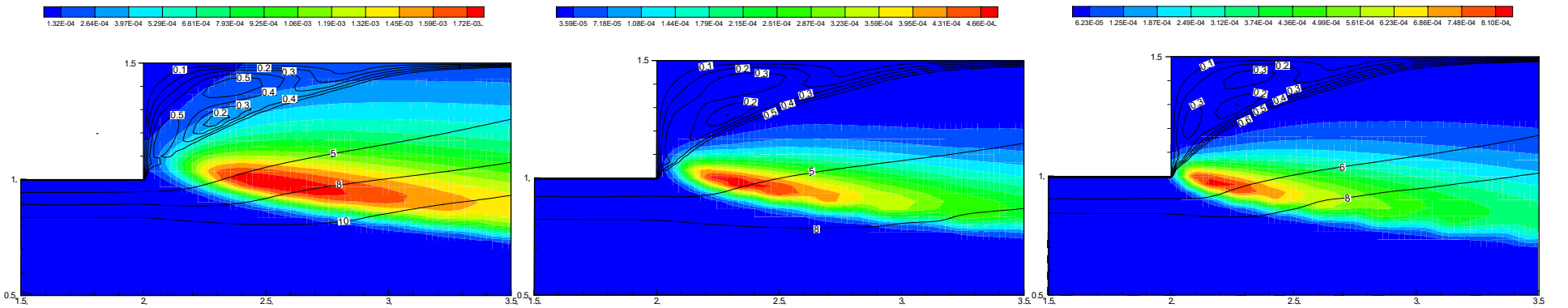
16

(a) Run 6: $v_j = 10 \ m/s$

(b) Run 7: $v_j = 15 \ m/s$

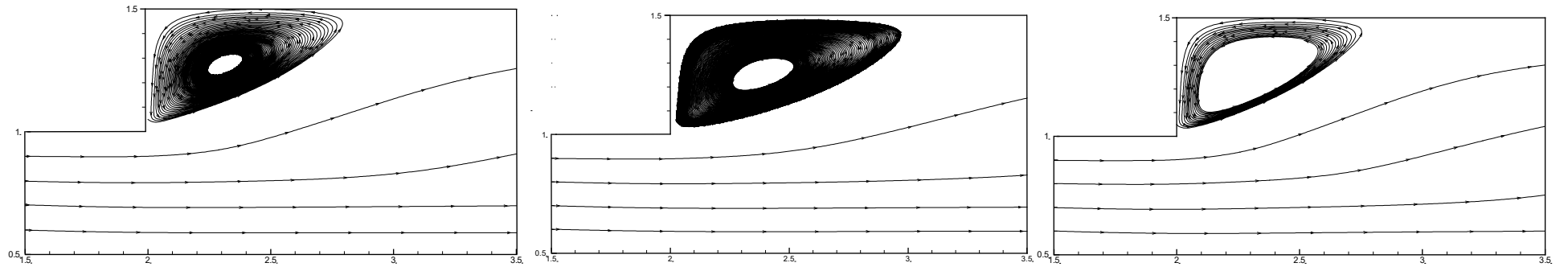(c) Run 10: $x_{H_2,j} = 0.3442$, $x_{O_2,j} = 0.0983$, $x_{N_2,j} = 0.5575$

(d) Run 12: $x_{H_2O,j} = 0.05$, $x_{O_2,j} = 0.0983$, $x_{N_2,j} = 0.5575$

(e) Run 16: equivalence ratio=0.5
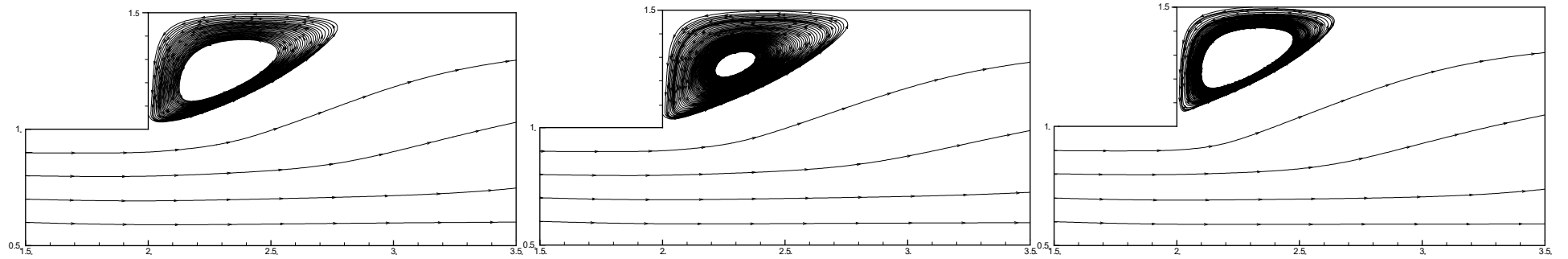
(f) Run 17: equivalence ratio=0.6

Fig 6. H mass fraction contours overlaid velocity level lines (black line) near the flame anchoring zone for stainless steel material

(a) Run 6: $v_j = 10 \ m/s$

(b) Run 7: $v_j = 15 \ m/s$

(c) Run 10: $x_{H_2,j} = 0.3442$, $x_{O_2,j} = 0.0983$, $x_{N_2,j} = 0.5575$

(d) Run 12: $x_{H_2O,j} = 0.05$, $x_{O_2,j} = 0.0983$, $x_{N_2,j} = 0.5575$

(e) Run 16: equivalence ratio=0.5

(f) Run 17: equivalence ratio=0.6

**Fig 7. the flow streamlines near the flame anchoring zone**

7.2 Effect of heat recirculation

The microchannel solids wall plays a key role on the combustion characteristics in the micro and meso channels by affecting the heat recirculation [47-49] as in other large combustors [50-52]. To verify the heat recirculation on the flame anchoring at the photovoltaic micro combustor, three solids (stainless steel, quartz (SiO_2), Inconel 625 and Silicon Carbide (SiC)) were chosen for the material of the combustor. The physical characteristics of solids are given in table 3. The simulation for equivalence ratio 0.5 was performed in the microcombustor for the materials selected.

Table 3 Properties of solid materials

Property	Stainless steel	Quartz	Inconel 625	Silicon Carbide
Density (gr/cm^3)	8.03	2.65	8.47	4.36
Specific heat (J/kg K)	502	730	647	650
Thermal conductivity (W/m. K)	16.27	1.5	29.6	20.7
Emissivity	0.85	0.92	0.71	0.90

The heat transfer map in the microchannel is depicted in Fig 8 at the combustor. The heat transfer is mapped in the microchannel step by showing the names as well as the direction of heat flux through the walls. The incoming hydrogen/air mixture receives heat from the microchannel interior walls (Q_1), igniting further downstream. The released heat from the combustion is partly transferred to the microchannel step vertical wall (Q_2) and partly from the interior horizontal wall by moving towards the outlet. The heat transferred to the step walls can be transferred by the solid material by conduction, providing the required heat (Q_1) for ignition of premixed H_2/N_2 mixture.
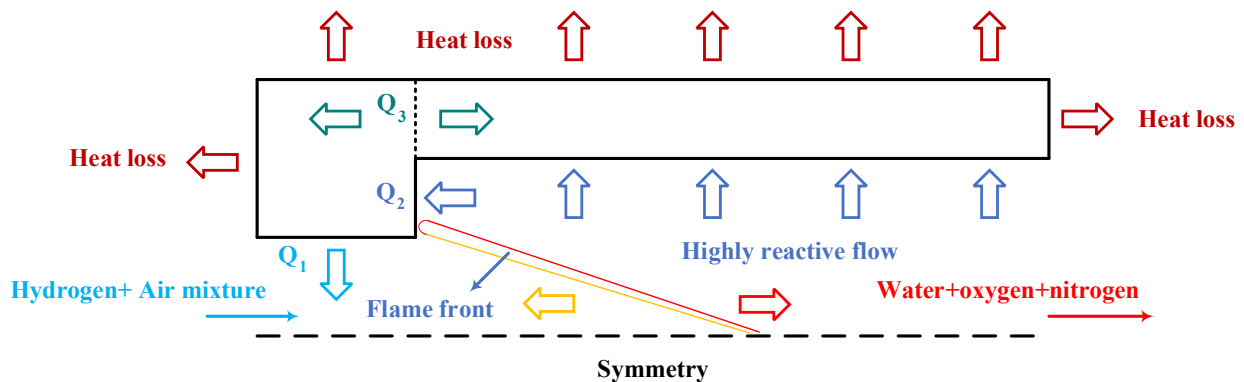
Fig 8 The heat transfer network blueprints in the microchannel combustor (the bold arrows indicate the direction of heat flux).

The temperature along the microchannel interior walls for different solid materials at equivalence ratio 0.5 confirms that the maximum wall temperatures lie in the step of the channel (not shown here). The maximum gas temperature depends on the thermal conductivity of solid materials which are 1617 K for quartz, 1628 K for Inconel 625, 1625 K for silicon carbide, 1626 K for stainless steel. These numbers show that flame maximum temperature increases with an increase of solid thermal conductivity. This trend conveys that the reaction rates improve with a larger thermal conductivity of the solid materials. This could happen as a result of heat recirculation by the reacted materials on the incoming fresh reactant. To approve the verity of this finding, the temperature profile of the upstream inner walls is shown in Fig 9.
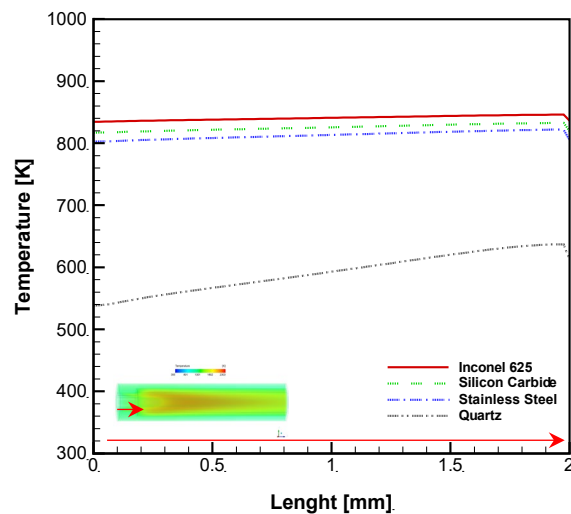
Fig 9 the temperature of combustor duct interior walls for different solid materials.

Indeed, more heat will be transferred longitudinally from the flame to the step vertical wall and from the downstream wall to the upstream wall. As a result, higher values in temperature profile are reasonable in the upstream walls with high thermal conductivity. This also leads to better preheat of incoming fresh reactants. Basically, the heat transfer is more near walls of combustors with higher thermal conductivities as a result of the bigger temperature differences between the wall and near-wall gas mixture. The heat fluxes through the inner walls (Q_1: Fig 8) are 140, 129, 127 and 77 kW/m^2 for Inconel 625, SiC, SS 310 and SiO$_2$, respectively. Consequently, the reactants receive more heat

in solid materials with higher thermal conductivity. The volume averaged gas mixture temperature before the reactant entered the downstream section of the microchannel ($T_{interior,\ ave}$ [K]) was 408, 399, 398, and 351 K for the metals from highest to lowest thermal conductivity, respectively. Table 4 gives a more descriptive scheme for heat transfer through walls with different solid materials. Table 4 gives a more comprehensive data regarding the heat transfer in the microchannel.

Table 4 Heat transfer specifications in microchannel for different materials

Material	Q_1 [kW/m^2]	Q_2 [kW/m^2]	Q_3 [kW/m^2]	$T_{interior,\ ave}$ [K]	$T_{channel,\ ave}$ [K]
Inconel 625	140	50.9	1.93	408	1200
Silicon Carbide	129	43.4	1.95	399	1183
Stainless steel	127	42.7	1.85	398	1187
Quartz	77	16.5	0.968	351	1149

When the mixture of hydrogen and air is flowing to the microchannel, some elementary reactions could be initiated in the narrow part of the channel due to the preheating effects Q_2. The main chemical reactions in the flame of the hydrogen are listed as follows [25]:

$$H + O_2 \ f \ OH + O \tag{R1}$$

$$O + H_2 \ f \ H + OH \tag{R2}$$

$$OH + H_2 \ f \ H + H_2O \tag{R3}$$

$$O + H_2O \ f \ OH + OH \tag{R4}$$

Fig 10 demonstrates the profiles of the Arrhenius rate of reactions R1, R2, R3, and R4 in the proximity of the upstream interior walls (x=0, y=0.975 mm, z=0-2 mm) for different solids at equivalence ratio 0.5. This graph shows that ignition begins at a place slightly before the reactants enter the extended part in the duct of the microchannel. The rate of reactions for a solid with a higher thermal conductivity was obtained plausibly higher which are for respectively Inconel 625, Silicon Carbide, Stainless Steel, and Quartz. For R4, the rate of reaction was obtained negative, meaning that the rate of R4 forward reaction dominates the rate of R4 forward reaction. The fact that the ignition

begun in the duct of the channel implies that heat recirculation, in general, has a remarkable influence on the initiation of the chain reactions for H_2/air premixed turbulent flame.
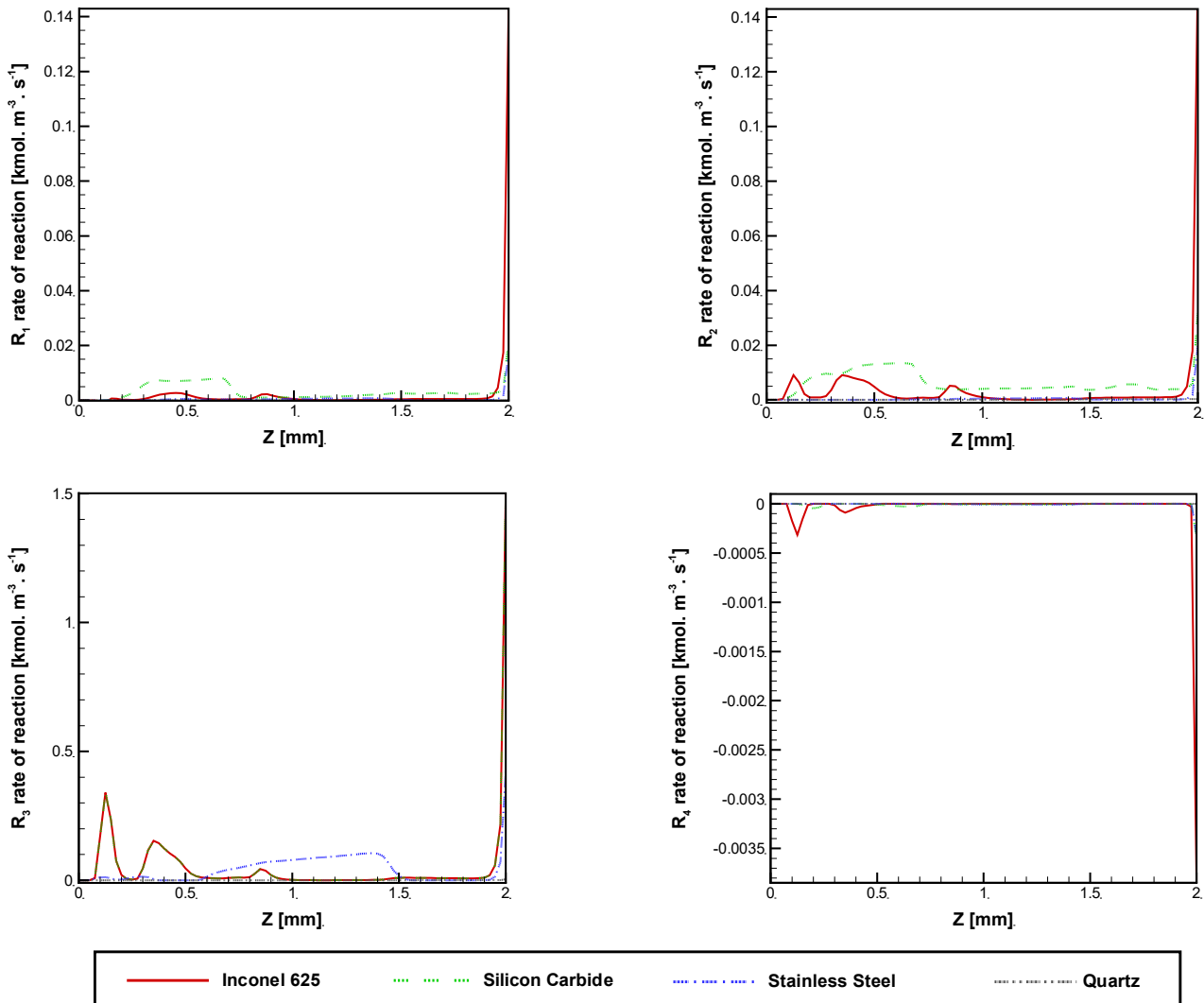
Fig 10 Arrhenius rate of reactions 1-4 in the vicinity of the interior upstream wall (x=0, y=0.975 mm, z=0-2 mm) for different solids at equivalence ratio=0.5.

The reaction rates are mainly influenced by heat recirculation in the cavity of the micro-combustor. Fig 11 depicts the trend of gas temperature and hydrogen mass fractions in the vicinity of the cavity walls (z=0.002025) at equivalence ratio 0.5 for different solids. The maximum temperature and H mass fractions are observed at the beginning of the wall and shifting towards the center of the channel. This trend implies that the burning velocity is higher for solid materials with higher thermal conductivity. As evident in the case of quartz, maximum values of both temperature and H mass fraction shifts towards the cavity wall center, becoming also more uniform compared to solids with higher thermal conductivities.
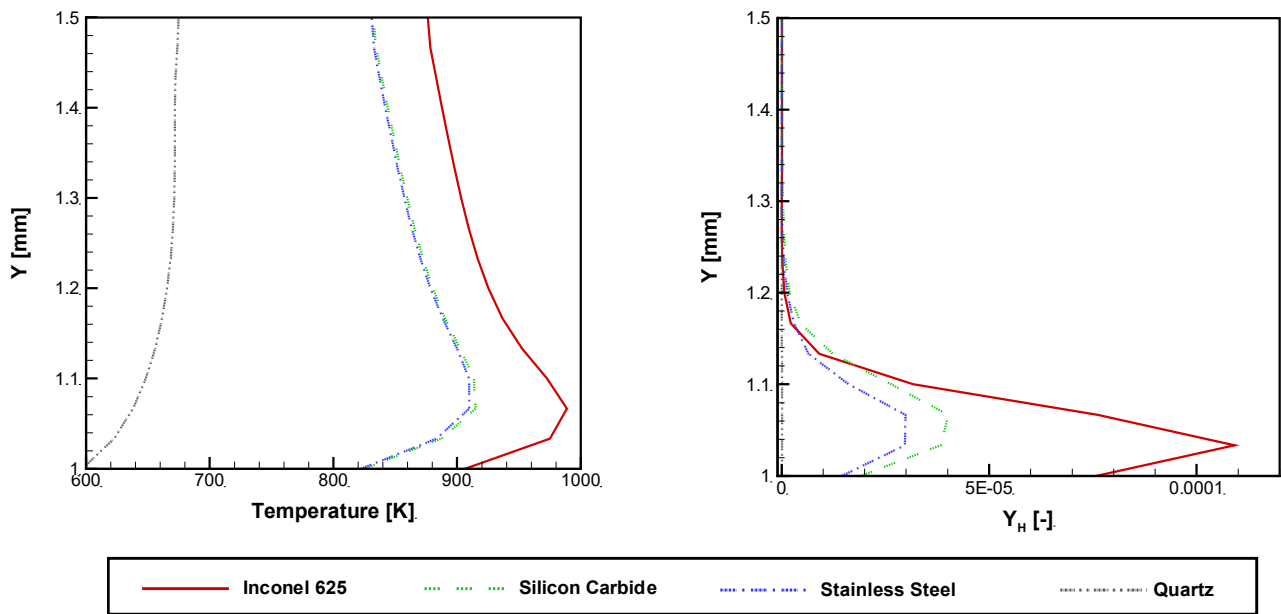
Fig 11 Temperature and H mass fraction (Y_H) profiles in the proximity of microchannel vertical step wall (z= 2.025 mm) for materials at equivalence ratio=0.5

As previously discussed, the heat recirculation near the step walls plays a vital role in the flame stabilization. To discuss it more, Fig 12 is given which shows the heat flux at the step vertical wall and difference between the step vertical wall and gas temperatures in the vicinity of it for x=3.025 mm. By comparing the relative level of heat fluxes and temperature differences for different solid materials, it can be seen that they could be completely different depending on the wall location. Near the bottom of the cavity, the heat flux for quartz is largest. Here, solids with the lowest thermal conductivities are more heat conductive. This is mainly because of the larger temperature difference obtained for these materials. The large temperature differences are owing to the lower thermal conductivities. The overall heat transfer flux from the hot flame in the step of microchannel to the cavity vertical walls (Q_2) are 50.9, 43.4, 42.7 and 16.5 kW/m^2 respectively for Inconel 645, Silicon Carbide, Stainless Steel, and quartz. The corresponding heat transfer fluxes are from the step vertical wall to the interior walls of the microchannel duct Q_3 1.93, 1.95, 1.85, and 0.968 w/m^2 for Inconel 625, silicon carbide, stainless steel, and quart, respectively. From these number, it can be concluded that the material with the biggest thermal conductivity (Inconel 625) obtain and transfer the highest rate of heat transfer to the interior walls at the duct of the microchannel. Therefore, the heat

recirculation effects for material with the higher thermal conductivity is bigger, leading to flame stabilization and possible flame anchoring in the channel step.
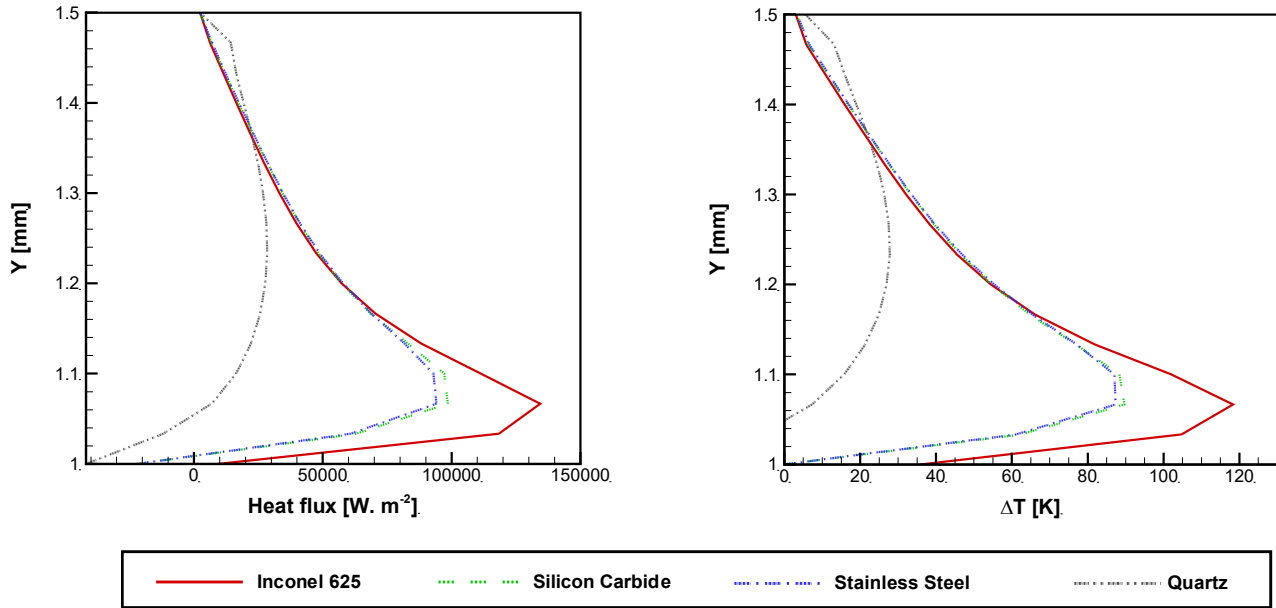
Fig 12 Heat flux from the hot gas (x = 3 mm) to the step vertical wall and temperature difference between vertical cavity wall and hot gas at z=2.025 mm for different solid materials at equivalence ratio 0.5.

7.3 Mass transport effect

The different mass diffusivities of species would influence the local concentration of gaseous mixture and local equivalence ratio in the combustion. This variation in concentration of species is called preferential transport effect [53, 54]. By evaluating the anchoring mechanism of premixed CH$_4$/air flame in a bluff-body combustor via high resolution laser diagnostics, Barlow et al. [53] defined a term called local equivalence ratio (f_{local}) to qualitatively evaluate the strong preferential transport effect that exists in the recirculation zone behind the bluff-body. Here, the preferential mass transport effect is analyzed using by two terms-1. equivalence ratio (f_{local}), and 2. mixture fraction (x_{local}). First the global definition of equivalence ratio is defined and used to analyze the mass transport effects and show how H$_2$/O$_2$ ratio changes in the microchannel

$$f_{local} = \frac{0.5X_{H_2}}{X_{O_2}}$$ 1

In this equation, X_i denotes the mole fraction of species i.

The spatial molar concentrations of species are different in the microchannel because of the occurrence of elementary reactions, and the different diffusivities because they highly depend on the type of material and temperature. Therefore, the equivalence ratio varies in the reacting flow. Fig 13 demonstrates the trend of the spatial equivalence ratio and temperatures along the axis (i.e., centerline) of the quartz microchannel. The spatial temperatures rise remarkably in the flame front of the premixed jet where it is 8, 9.5 and 12.5 mm downstream of the microchannel inlet for equivalence ratios 0.7, 0.6, and 0.5, respectively. The ER starts going down drastically in the flame front. This phenomenon was previously confirmed in CH_4/air. A local equivalence ratio defined by Kedia [54] and Barlow [53] goes down in a similar way and gradually returning to the incoming equivalence ratio behind the flame front.
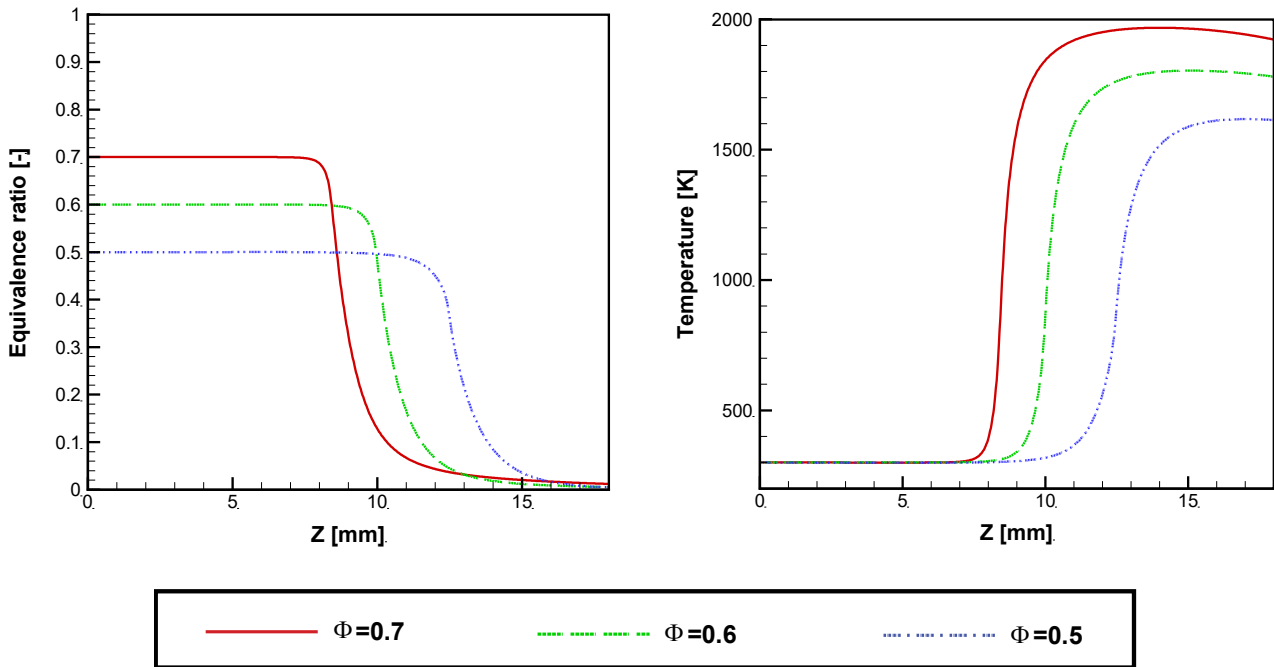
Fig 13 The equivalence ratio and gas temperature along the axis of the quartz combustor for three different equivalence ratios 0.5, 0.6, and 0.7
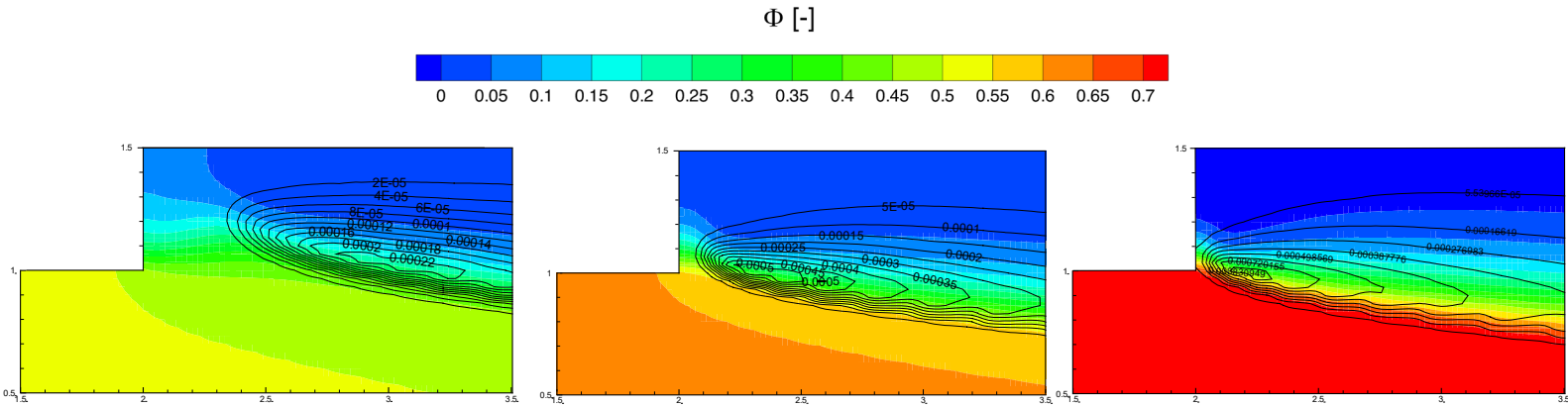
The contour plots of the equivalence ratio accompanying with the velocity lines for equivalence ratio 0.5, 0.6, and 0.7 of the quartz combustor are illustrated in Fig 14. From this figure, it can be readily seen that there is a sharp gradient in equivalence ratio in the vicinity of the step wall. This

sharp gradient in equivalence ratio leads to recirculation of unreacted materials from downstream and flame stabilization in the microchannel step.
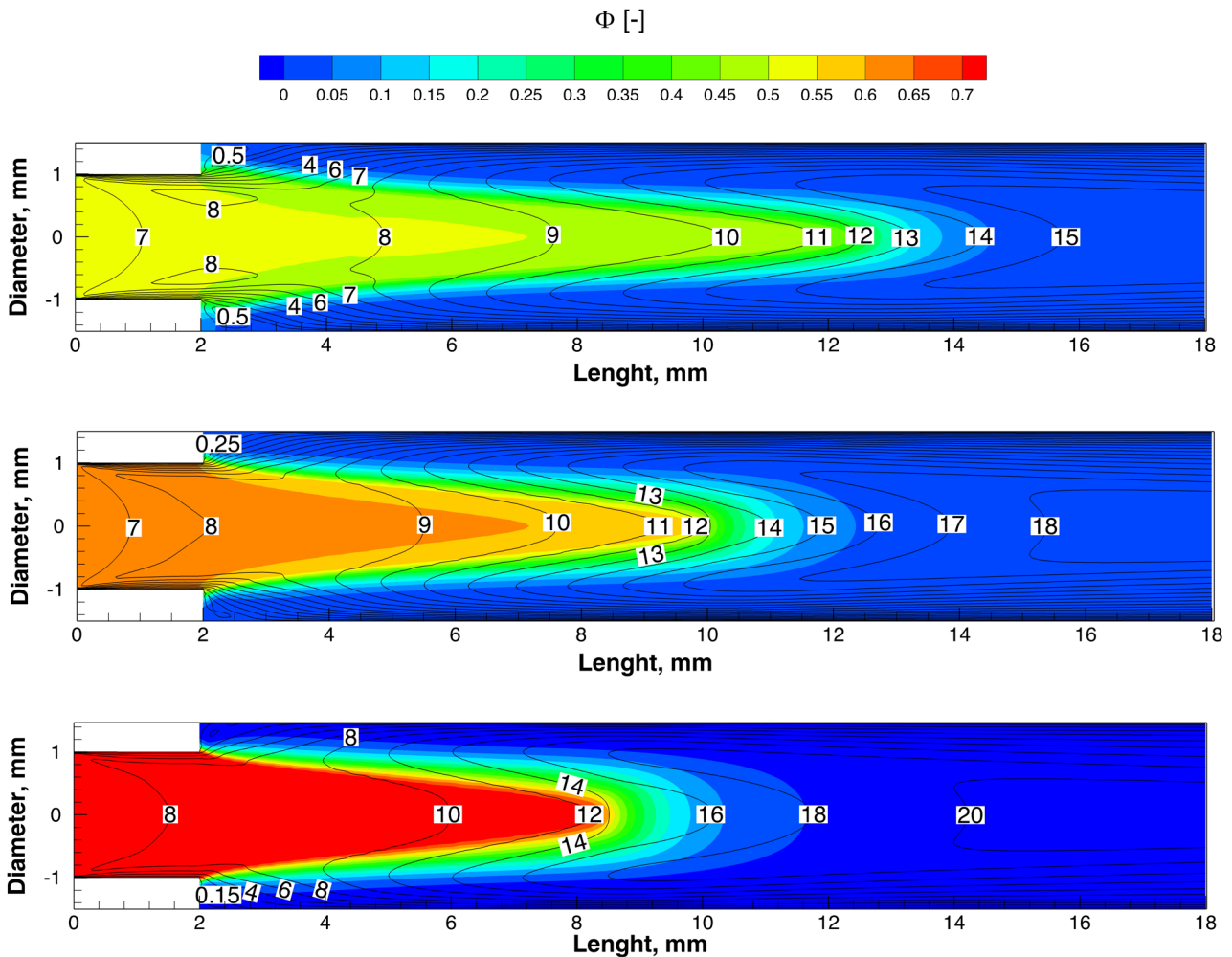

Fig 14 The contour plots of equivalence ratios overlaid with velocity lines for three inlet equivalence ratios 0.5, 0.6, and 0.7 in quartz combustor.

Fig 15 gives the contour plots of equivalence ratio ratios overlaid with H mass fraction near the flame anchoring location. Evidently, the equivalence ratio is larger near the flame roots. Although the high mass fractions of the H are concentrated in the central part of the flame forming the anchoring location, a part of low H mass fraction lines are observed in the step of the channel where equivalence ratio and as a result H_2 mass fractions are low. The combustion species in the partially reacted flow in this part diffuse to the fresh reactant coming from the inlet forming a recirculation in the vicinity microchannel step. The finally eventuate to the flame stabilization in the microchannel step.

Fig 15 The contour plots of equivalence ratios overlaid with H mass fraction for three inlet equivalence ratios 0.5, 0.6, and 0.7 in quartz combustor.

For a better understanding of the mechanism of flame anchoring, the radial equivalence ratio, fluid velocity, and gas temperature profiles at different axial distances (i.e., x=2.5 mm, 3 mm, 3.5 mm and 4.0 mm) of the microchannel are shown in Fig 16 for equivalence ratio 0.5. The flame front in these graphs marked with a drastic decrease in velocity and equivalence ratio, and a significant increase of temperatures.
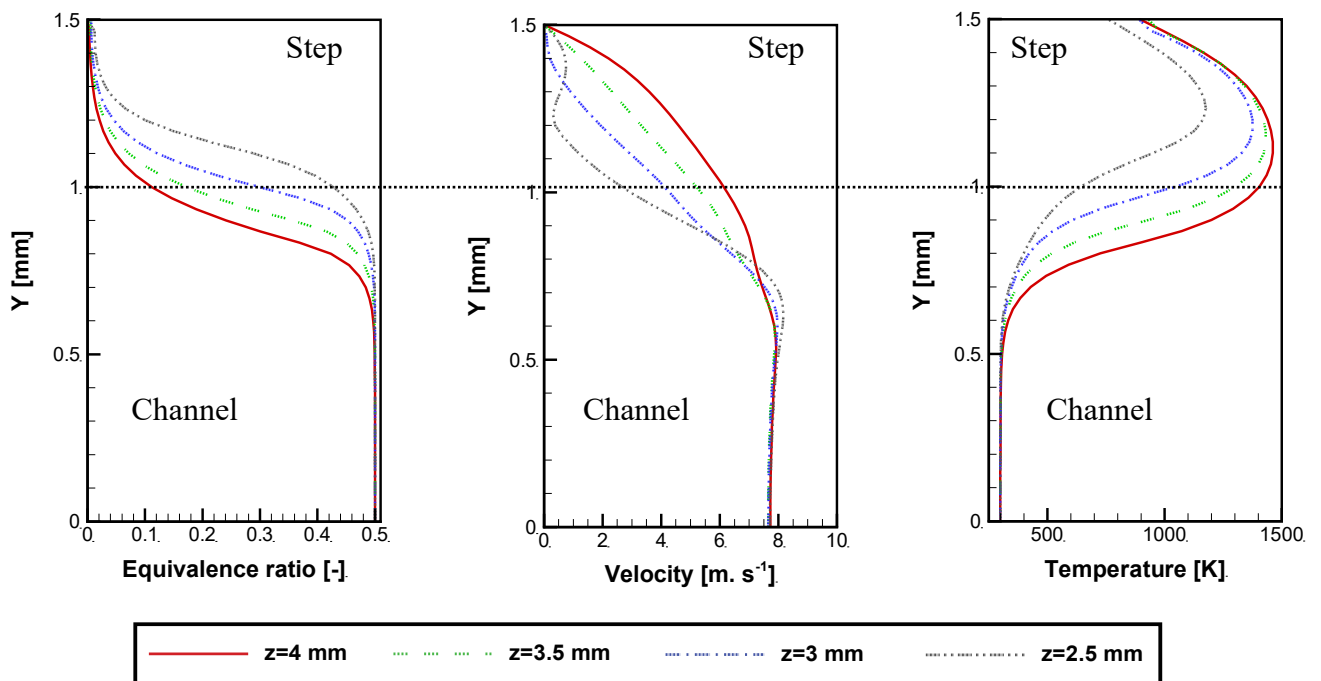
Fig 16 The equivalence ratio, velocity level lines and gas temperature profiles along the half of the channel ($0 \text{ mm} \pounds \text{ y} \pounds 1.5 \text{ mm}$) in the quartz combustor at four different distances 2.5, 3, 3.5 and 4 mm downstream of the jet inlet (equivalence ratio 0.5).

The nearest distance to the step wall corresponds to see z=2.5 mm. The flame front is observed at radial distance 0.8 mm in the vicinity of the microchannel step. The maximum values of the temperature are observed at the step of channel confirming the occurrence of the combustion and effective role of walls in the flame stabilization. Indeed, the cavity in the microchannel intensifies the dimensionality of the flow along the radial and axial flow, thereby leading to the formation of an area with low local velocities. The gradient in the velocity of the flow in the cavity can instigate the transport effect of combustion species and flame evolution from the step walls. This effect was also observed in other flames [55].

To analyze better the mass transport effect, now the affinity of H_2 for O is analyzed here. To this end, the local mixture fraction is defined which shows the ratio of hydrogen molecules to O atoms as flows:

$$x_{local} = \frac{0.5(X_{H_2} + X_{H_2O} + X_{H_2O_2}) + 0.25(X_H + X_{OH} + X_{HO_2})}{0.5(X_O + X_{H_2O} + X_{OH} + X_{NO} + X_{N_2O}) + X_{O_2} + X_{HO_2} + X_{H_2O_2} + X_{NO_2}} \qquad 2$$

For the case of quartz combustor working with ER=0.7 in premixed hydrogen flame, the contour plots of $x_{local} - x_{inlet}$ is shown in Fig 17. The $x_{local} - x_{inlet}$ increases in the vicinity of the step wall by strong two-dimensionality of flow in the cavity. On the inner part of the flame, the $x_{local} - x_{inlet}$ is much larger than the outer part of the flame. The recirculation zone of material near the cavity walls from the outer to inner flame boundary results in this different affinity of hydrogen molecules to oxygen atoms which caused the flame stabilizations.
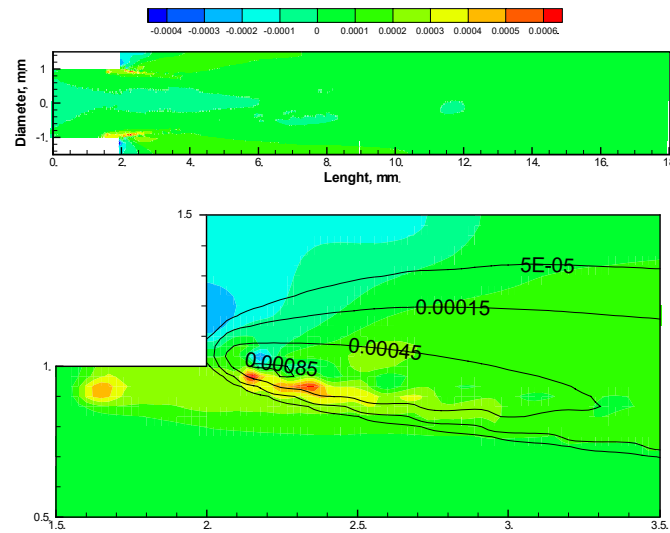
Fig 17 The contour plots of X_{local} - X_{inlet} overall and overlaid with H mass fraction for inlet equivalence ratios 0.7 in quartz combustor.

The ignition can be further investigated using precursor species. The H, HO_2, and H_2O_2 are ignition marker species [8, 56] which their radial mass fraction profiles are shown in Fig 18 at different axial distances for quartz combustor with initial equivalence ratio=0.7. It can be readily seen that the ignition process began in the vicinity of the step walls. During the radical build-up state, the precursor species accumulate on the outer diffusion layer of the flame where the equivalence ratio is rather low (a little below the step). This can also result in a gradual increase in the temperature of the mixture until the ignition. Finally, when the ignition begins, the concentrations of precursor species decrease that should be at different rates. Fig 18 demonstrates that precursor concentrations are high near the vicinity wall which could also show that radical buildup, thermal runaway, and flame root are all started from here. In this case (ER=0.7 for quartz combustor), although the flame does not perfectly locate in the step of the channel, the role of step in the ignition cannot be gainsaid as it transfers the heat from the combusted materials to the interior walls as well as the main cause of low velocity and recirculation zone in the channel.
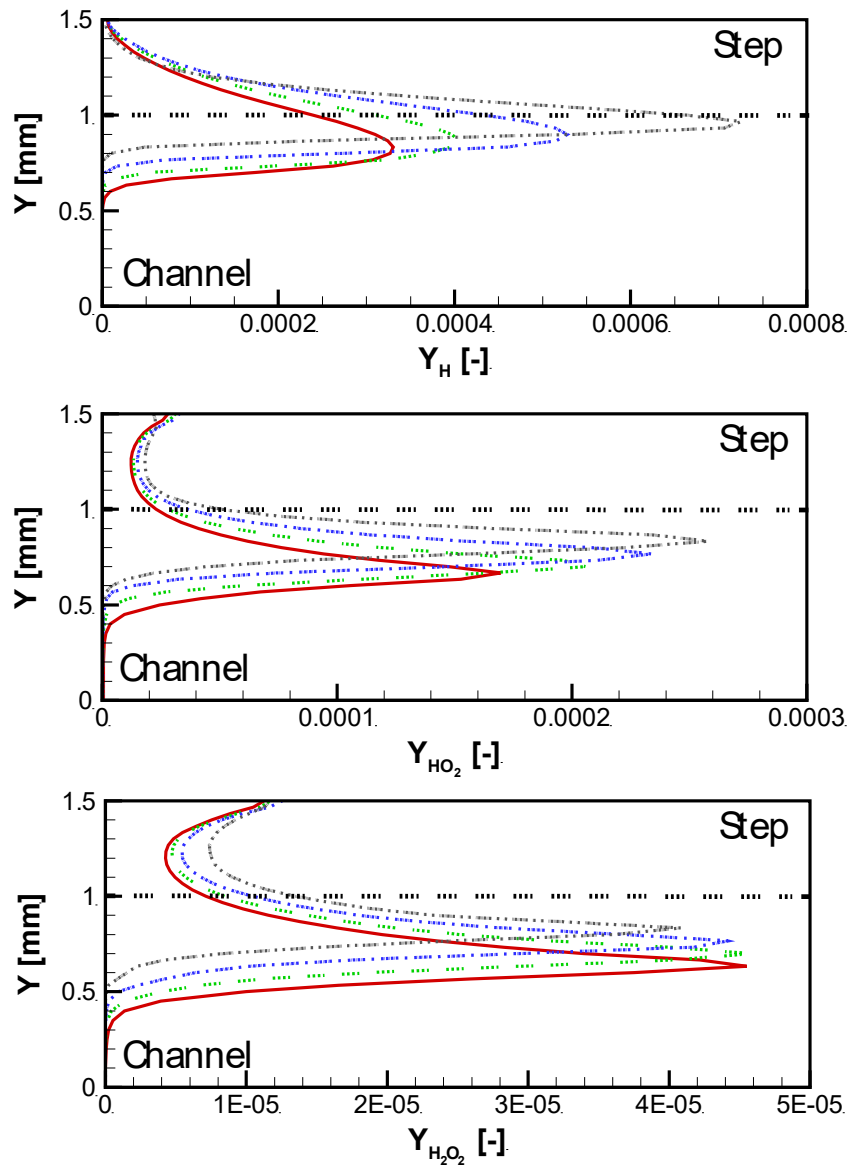
Fig 18 The mass fractions profiles of precursor species (H, HO₂, H₂O₂)along the half of the channel ($0 \text{ mm} \pounds \text{ y} \pounds 1.5 \text{ mm}$ **) in the quartz combustor at four different distances 2.5, 3, 3.5 and 4 mm downstream of the jet inlet (equivalence ratio 0.7).**

8. Conclusions

The photovoltaic cells are small energy gensets as they are compact, efficient, and promising. In this study, the microcombustion of hydrogen premixed flame is simulated and analyzed to provide an in-depth insight into the mechanism of flame anchoring. The influence of the different operating points including jet temperature, water content, hydrogen content, nitrogen content, oxygen content, jet velocities, equivalence ratio and material of the combustor are investigated. The main conclusions are as follows :

1) Depending on the operating point investigated, the flame anchoring root was observed in either the microchannel step wall or interior walls.

2) The formation of recirculation zone with low local velocity, as a result, heat recirculation effect, heat loss from the flame tip and transport and circulation of the combustion species in the step of the channel are major contributing factors in the flame formation and stabilization in the microchannel.

3) The recirculation zone with two opposing longitudinal velocity components leads to the occurrence of radical build-up state near the cavity wall.

4) The heat recirculated and obtained from the step wall and recirculating materials result in the early occurrence of the chain reactions beside the upstream interior walls. This also leads to more intense reactions near step walls and flame anchoring.

5) For better investigating the heat recirculation, combustion in the microchannel with different solid materials is simulated. The flame anchoring place is closer to the cavity walls in combustors with high thermal conductivities.

6) The difference in both the mixture fraction and equivalence ratio of the microchannel cavity is as a result of the different velocities, two-dimensionality of the flow and the different diffusivities of the species. This difference makes the cavity of the microchannel a radical pool, leading to the flame anchoring in this area.

This research makes a direct leeway towards the improvement of the photovoltaic cell combustors by showing the main flame anchoring mechanisms. The occurrence of radical buildup phase state near the cavity walls as well as recirculation of materials there could result in the significant formation of pollutants, necessitating more research and intricate analysis of hydrogen flame in this combustor using more accurate unsteady numerical schemes. The high residence time of materials traped in the recirculation zone neat the cavity wall for this combustor may lead to a significant NO_X.

9. References

[1] Maruta K. Micro and mesoscale combustion. Proceedings of the Combustion Institute. 2011;33(1):125-50.

[2] Fernandez-Pello AC. Micropower generation using combustion: issues and approaches. Proceedings of the combustion institute. 2002;29(1):883-99.

[3] Sirignano WA, Pham TK, Dunn-Rankin D. Miniature-scale liquid-fuel-film combustor. Proceedings of the Combustion Institute. 2002;29(1):925-31.

[4] Akhtar S, Khan MN, Kurnia JC, Shamim T. Investigation of energy conversion and flame stability in a curved micro-combustor for thermo-photovoltaic (TPV) applications. Applied Energy. 2017;192:134-45.

[5] Sitzki L, Borer K, Wussow S, Maruta E, Ronney P. Combustion in microscale heat-recirculating burners. Conference Combustion in microscale heat-recirculating burners. p. 1087.

[6] Kuo C-H, Ronney P. Numerical modeling of non-adiabatic heat-recirculating combustors. Proceedings of the Combustion Institute. 2007;31(2):3277-84.

[7] Kim NI, Kato S, Kataoka T, Yokomori T, Maruyama S, Fujimori T, et al. Flame stabilization and emission of small Swiss-roll combustors as heaters. Combustion and Flame. 2005;141(3):229-40.

[8] Bazooyar B, Shariati A, Hashemabadi SH. Turbulent non-premixed combustion of rapeseed methyl ester in a free shear swirl air flow. Industrial & Engineering Chemistry Research. 2016;55(45):11645-63.

[9] Leu C-H, King S-C, Huang J-M, Chen C-C, Tzeng S-S, Lee C-I, et al. Visible images of the catalytic combustion of methanol in a micro-channel reactor. Chemical Engineering Journal. 2013;226:201-8.

[10] Wan J, Fan A, Maruta K, Yao H, Liu W. Experimental and numerical investigation on combustion characteristics of premixed hydrogen/air flame in a micro-combustor with a bluff body. International Journal of Hydrogen Energy. 2012;37(24):19190-7.

[11] Yang W, Chou S, Shu C, Li Z, Xue H. Combustion in micro-cylindrical combustors with and without a backward facing step. Applied Thermal Engineering. 2002;22(16):1777-87.

[12] Boyarko GA, Sung C-J, Schneider SJ. Catalyzed combustion of hydrogen–oxygen in platinum tubes for micro-propulsion applications. Proceedings of the Combustion Institute. 2005;30(2):2481-8.

[13] Zhou J, Wang Y, Yang W, Liu J, Wang Z, Cen K. Combustion of hydrogen–air in catalytic micro-combustors made of different material. International Journal of hydrogen energy. 2009;34(8):3535-45.

[14] Choi W, Kwon S, Shin HD. Combustion characteristics of hydrogen–air premixed gas in a sub-millimeter scale catalytic combustor. International journal of hydrogen energy. 2008;33(9):2400-8.

[15] Bazooyar B, Shariati A, Khosravi-Nikou M, Hashemabadi SH. Numerical analysis of nitrogen oxides in turbulent lifted H2/N2 cabra jet flame issuing into a vitiated coflow. International Journal of Hydrogen Energy. 2019;44(26):13932-52.

[16] Bazooyar B, Darabkhani HG. Design and numerical analysis of a 3 kWe flameless microturbine combustor for hydrogen fuel. International Journal of Hydrogen Energy. 2019;44(21):11134-44.

[17] Wan J, Fan A, Yao H, Liu W, Gou X, Zhao D. The impact of channel gap distance on flame splitting limit of H2/air mixture in microchannels with wall cavities. international journal of hydrogen energy. 2014;39(21):11308-15.

[18] Wan J, Yang W, Fan A, Liu Y, Yao H, Liu W, et al. A numerical investigation on combustion characteristics of H2/air mixture in a micro-combustor with wall cavities. international journal of hydrogen energy. 2014;39(15):8138-46.

[19] Li Y-H, Chen G-B, Hsu H-W, Chao Y-C. Enhancement of methane combustion in microchannels: effects of catalyst segmentation and cavities. Chemical Engineering Journal. 2010;160(2):715-22.

[20] Wan J, Fan A, Liu Y, Yao H, Liu W, Gou X, et al. Experimental investigation and numerical analysis on flame stabilization of CH4/air mixture in a mesoscale channel with wall cavities. Combustion and Flame. 2015;162(4):1035-45.

[21] Nehe P, Kumar S. Methanol reformation for hydrogen production from a single channel with cavities. International Journal of Hydrogen Energy. 2013;38(30):13216-29.

[22] Faramarzpour H, Mazaheri K, Alipoor A. Effect of backward facing step on radiation efficiency in a micro combustor. International Journal of Thermal Sciences. 2018;132:129-36.

[23] Peng Q, Jiaqiang E, Yang WM, Xu H, Chen J, Zhang F, et al. Experimental and numerical investigation of a micro-thermophotovoltaic system with different backward-facing steps and wall thicknesses. Energy. 2019;173:540-7.

[24] Wan J, Fan A, Yao H, Liu W. Flame-anchoring mechanisms of a micro cavity-combustor for premixed H2/air flame. Chemical Engineering Journal. 2015;275:17-26.

[25] Li J, Zhao Z, Kazakov A, Dryer FL. An updated comprehensive kinetic model of hydrogen combustion. International journal of chemical kinetics. 2004;36(10):566-75.

[26] Bazooyar B, Ebrahimzadeh E, Jomekian A, Shariati A. NOx Formation of Biodiesel in Utility Power Plant Boilers. Part A: Influence of Fuel Characteristics. Energy & Fuels. 2014;28(6):3778-92.

[27] Bazooyar B, Hashemabadi SH, Shariati A. NOX formation of biodiesel in utility power plant boilers; Part B. Comparison of NO between biodiesel and petrodiesel. Fuel. 2016;182:323-32.

[28] Bazooyar B, Shariati A, Hashemabadi SH. Characterization and Reduction of NO during the Combustion of Biodiesel in a Semi-industrial Boiler. Energy & Fuels. 2015;29(10):6804-14.

[29] Bazooyar B, Jomekian A, Shariati A. Analysis of the formation and interaction of nitrogen oxides in a rapeseed methyl ester nonpremixed turbulent flame. Energy & Fuels. 2017;31(8):8708-21.

[30] Bazooyar B, Ghorbani A, Shariati A. Physical properties of methyl esters made from alkali-based transesterification and conventional diesel fuel. Energy Sources, Part A: Recovery, Utilization, and Environmental Effects. 2015;37(5):468-76.

[31] Bazooyar B, Ghorbani A, Shariati A. Combustion performance and emissions of petrodiesel and biodiesels based on various vegetable oils in a semi industrial boiler. Fuel. 2011;90(10):3078-92.

[32] Ghorbani A, Bazooyar B. Optimization of the combustion of SOME (soybean oil methyl ester), B5, B10, B20 and petrodiesel in a semi industrial boiler. Energy. 2012;44(1):217-27.

[33] Ghorbani A, Bazooyar B, Shariati A, Jokar SM, Ajami H, Naderi A. A comparative study of combustion performance and emission of biodiesel blends and diesel in an experimental boiler. Applied Energy. 2011;88(12):4725-32.

[34] Jiang D, Yang W, Chua KJ, Ouyang J. Thermal performance of micro-combustors with baffles for thermophotovoltaic system. Applied Thermal Engineering. 2013;61(2):670-7.

[35] Jiang D, Yang W, Chua KJ, Ouyang J, Teng J. Effects of H2/CO blend ratio on radiated power of micro combustor/emitter. Applied Thermal Engineering. 2015;86:178-86.

[36] Tang A, Xu Y, Pan J, Yang W, Jiang D, Lu Q. Combustion characteristics and performance evaluation of premixed methane/air with hydrogen addition in a micro-planar combustor. Chemical Engineering Science. 2015;131:235-42.

[37] Tang A, Pan J, Yang W, Xu Y, Hou Z. Numerical study of premixed hydrogen/air combustion in a micro planar combustor with parallel separating plates. International Journal of Hydrogen Energy. 2015;40(5):2396-403.

[38] Wenming Y, Dongyue J, Kenny CKY, Dan Z, Jianfeng P. Combustion process and entropy generation in a novel microcombustor with a block insert. Chemical Engineering Journal. 2015;274:231-7.

[39] Jiaqiang E, Zuo W, Liu X, Peng Q, Deng Y, Zhu H. Effects of inlet pressure on wall temperature and exergy efficiency of the micro-cylindrical combustor with a step. Applied Energy. 2016;175:337-45.

[40] Olm C, Zsély IG, Pálvölgyi R, Varga T, Nagy T, Curran HJ, et al. Comparison of the performance of several recent hydrogen combustion mechanisms. Combustion and Flame. 2014;161(9):2219-34.

[41] Kéromnès A, Metcalfe WK, Heufer KA, Donohoe N, Das AK, Sung C-J, et al. An experimental and detailed chemical kinetic modeling study of hydrogen and syngas mixture oxidation at elevated pressures. Combustion and Flame. 2013;160(6):995-1011.

[42] Ó Conaire M, Curran HJ, Simmie JM, Pitz WJ, Westbrook CK. A comprehensive modeling study of hydrogen oxidation. International journal of chemical kinetics. 2004;36(11):603-22.

[43] Konnov AA. Remaining uncertainties in the kinetic mechanism of hydrogen combustion. Combustion and Flame. 2008;152(4):507-28.

[44] Hong Z, Davidson DF, Hanson RK. An improved H2/O2 mechanism based on recent shock tube/laser absorption measurements. Combustion and Flame. 2011;158(4):633-44.

[45] Davis SG, Joshi AV, Wang H, Egolfopoulos F. An optimized kinetic model of H2/CO combustion. Proceedings of the Combustion Institute. 2005;30(1):1283-92.

[46] Burke MP, Chaos M, Ju Y, Dryer FL, Klippenstein SJ. Comprehensive H2/O2 kinetic model for high-pressure combustion. International Journal of Chemical Kinetics. 2012;44(7):444-74.

[47] Wan J, Fan A, Yao H, Liu W. Effect of thermal conductivity of solid wall on combustion efficiency of a micro-combustor with cavities. Energy Conversion and Management. 2015;96:605-12.

[48] Kaisare N, Vlachos D. Optimal reactor dimensions for homogeneous combustion in small channels. Catalysis Today. 2007;120(1):96-106.

[49] Norton DG, Vlachos DG. A CFD study of propane/air microflame stability. Combustion and Flame. 2004;138(1-2):97-107.

[50] Bazooyar B, Hallajbashi N, Shariati A, Ghorbani A. An investigation of the effect of input air upon combustion performance and emissions of biodiesel and diesel fuel in an experimental boiler. Energy Sources, Part A: Recovery, Utilization, and Environmental Effects. 2014;36(4):383-92.

[51] Bazooyar B, Shariati A. A comparison of the emission and thermal capacity of methyl ester of corn oil with diesel in an experimental boiler. Energy Sources, Part A: Recovery, Utilization, and Environmental Effects. 2013;35(17):1618-28.

[52] Bazooyar B, Shariati A, Hashemabadi SH. Economy of a utility boiler power plant fueled with vegetable oil, biodiesel, petrodiesel and their prevalent blends. Sustainable Production and Consumption. 2015;3:1-7.

[53] Barlow RS, Dunn MJ, Sweeney MS, Hochgreb S. Effects of preferential transport in turbulent bluff-body-stabilized lean premixed CH4/air flames. Combustion and Flame. 2012;159(8):2563-75.

[54] Kedia KS, Ghoniem AF. The anchoring mechanism of a bluff-body stabilized laminar premixed flame. Combustion and flame. 2014;161(9):2327-39.

[55] Katta V, Roquemore WM. C/H atom ratio in recirculation-zone-supported premixed and nonpremixed flames. Proceedings of the Combustion Institute. 2013;34(1):1101-8.

[56] Irannejad A, Banaeizadeh A, Jaberi F. Large eddy simulation of turbulent spray combustion. Combustion and Flame. 2015;162(2):431-50.